How to cite: *Angew. Chem. Int. Ed.* **2024**, *63*, e202402693
doi.org/10.1002/anie.202402693

Nanophotocatalysts

Metal–Organic Framework-Based Hetero-Phase Nanostructure Photocatalysts with Molecular-Scale Tunable Energy Levels

Kuo Yuan[+], Zongyang Liu[+], Zhuang Yan[+], Qinbai Yun, Tianqun Song, Jun Guo, Xiaotao Zhang, Dichang Zhong,* Zhiyong Tang, Tongbu Lu,* and Wenping Hu**

Abstract: As an effective method to modulate the physicochemical properties of materials, crystal phase engineering, especially hetero-phase, plays an important role in developing high-performance photocatalysts. However, it is still a huge challenge but significant to construct porous hetero-phase nanostructures with adjustable band structures. As a kind of unique porous crystalline materials, metal–organic frameworks (MOFs) might be the appropriate candidate, but the MOF-based hetero-phase is rarely reported. Herein, we developed a secondary building unit (SBU) regulating strategy to prepare two crystal phases of Ti-MOFs constructed by titanium and 1,4-dicarboxybenzene, i.e., COK and MIL-125. Besides, COK/MIL-125 hetero-phase was further constructed. In the photocatalytic hydrogen evolution reaction, COK/MIL-125 possessed the highest H_2 yield compared to COK and MIL-125, ascribing to the Z-Scheme homojunction at hetero-phase interface. Furthermore, by decorating with amino groups (i.e., NH_2-COK/NH_2-MIL-125), the light absorbing capacity was broadened to visible-light region, and the visible-light-driven H_2 yield was greatly improved. Briefly, the MOF-based hetero-phase possesses periodic channel structures and molecularly adjustable band structures, which is scarce in traditional organic or inorganic materials. As a proof of concept, our work not only highlights the development of MOF-based hetero-phase nanostructures, but also paves a novel avenue for designing high-performance photocatalysts.

Introduction

As an interdisciplinary subject in chemistry, pharmacology, physics and material science, crystal phase engineering has been deeply studied for a long time in organic and inorganic materials, and is full of fundamental and practical significance.[1] In the field of organic solids, crystal phase engineering is dominated by modulating the arrangement of organic molecules, which directly influences their band structures, electron-phonon couplings, interlayer electronic couplings and other intrinsic properties.[2] Hence, crystal phase engineering plays an important role in regulating the performance of organic optoelectronic devices, such as nonlinear optics, LED, FET, solar cell and so on.[3] In contrast, the crystal phase of inorganic materials is derived from the atomic arrangement or stacking sequence.[4] Taking transition metal dichalcogenides (TMDs) as a typical example, the 1T, 1T' and 2H phases of MoS_2 with different atomic arrangements exhibit conducting, semimetallic and semiconducting properties, respectively.[5] Besides, as for semiconducting metal oxides, the rutile and anatase phases of TiO_2 possess different energy levels, and the Z-scheme junction in rutile/anatase TiO_2 hetero-phase is beneficial for facilitating the separation of photogenerated electrons and holes, which improves the photocatalytic activity.[6]

Clearly, in crystal phase engineering, organic solids and inorganic materials possess their unique advantages, respectively. The band structures of organic materials can be precisely regulated at the molecular scale.[7] The different atomic arrangements of inorganic materials can affect the coordination environment of catalytic sites, which plays an

[*] Prof. Dr. K. Yuan,[+] Z. Liu,[+] Dr. T. Song, Prof. Dr. D. Zhong, Prof. Dr. T. Lu
Institute for New Energy Materials and Low Carbon Technologies, School of Materials Science & Engineering, Tianjin University of Technology, 300384 Tianjin, China
E-mail: yuankuo@email.tjut.edu.cn
dczhong@email.tjut.edu.cn
tongbulu@tjut.edu.cn

Prof. Dr. K. Yuan,[+] Dr. T. Song, Prof. Dr. X. Zhang, Prof. Dr. W. Hu
Department of Chemistry, School of Science & Key Laboratory of Organic Integrated Circuits, Ministry of Education, Tianjin University, 300072 Tianjin, China
E-mail: huwp@tju.edu.cn

Prof. Dr. K. Yuan,[+] Dr. T. Song
Key Laboratory of Advanced Energy Materials Chemistry (Ministry of Education), Nankai University, 300071 Tianjin, China

Z. Yan,[+] Prof. Dr. Z. Tang
CAS Key Laboratory of Nanosystem and Hierarchical Fabrication, National Center for Nanoscience and Technology, 100190 Beijing, China

Prof. Dr. Q. Yun
Department of Chemical and Biological Engineering & Energy Institute, The Hong Kong University of Science and Technology, Kowloon, Hong Kong, China This address is complete. There is no official postal code for Hong Kong.

Prof. Dr. J. Guo
State Key Laboratory of Separation Membranes and Membrane Processes, School of Chemistry, Tiangong University, 300387 Tianjin, China

Z. Yan,[+] Prof. Dr. Z. Tang
University of Chinese Academy of Sciences, 100049 Beijing, China

[+] These authors contributed equally to this work.

important role in optimizing their catalytic performance.[8] In practical applications, hetero-phase composites not only combine advantages of different phases, but also possess synergistic effect of two phases, which exhibits superior performance than pure phases. Hence, more and more attention has been paid on the design and construction of hetero-phase structures. For combining the advantages of organic and inorganic materials, it is a reliable and effective approach to construct inorganic-organic hybrid hetero-phase nanostructures (Figure 1 and Scheme S1). However, most of them are based on coordination polymers (CPs) without periodic channel structures, impeding their further development especially in catalysis.[9] As a type of inorganic-organic hybrids, metal–organic frameworks (MOFs) possess periodic porous structures, excellent compatibility, tailorable functionality and other advantages, and hence have been widely applied in various fields.[10] As for MOFs, their crystal phases are identified as different crystal structures composed of the same metal ions and organic ligands, which are also named as framework isomers.[11] In recent decades, a large number of crystal structures of MOFs and diverse types of MOF-based composites have been designed and synthesized.[12] However, the hetero-phase nanostructure of MOFs is still rarely reported so far due to the lack of synthetic strategies for different phases of MOFs. Normally, the different crystal phases of MOFs are prepared by slightly twisting the crystal structures, which can regulate the catalytic performance to some extent.[13] As for the preparation of crystal phases with larger difference in lattice parameters, it is still a huge challenge, but might bring new perspectives to practical applications.

Given the inorganic-organic hybrid property, the crystal phase of MOFs is heavily dependent on the coordination configuration and structures of organic ligands.[14] As the important metal nodes in frameworks, secondary building units (SBUs) not only greatly influence the coordination configuration which directly regulates the crystal structure of MOFs, but also affect their intrinsic properties (e.g., catalytic properties and conductivity).[15] SBUs endow framework with unsaturated coordination metals as active sites for catalysis.[16] Besides, the conductivity of framework is heavily dependent on the dimension of SBUs. The chain-based MOFs possess similar conductivity with nanoscale metal oxides, but the conductivity of cluster-based counterpart is negligible.[17] Based on these, it might be an effective and reliable approach to regulate the crystal phases of MOFs via changing SBUs (Figure 1), which can effectively optimize the performance of MOFs in multitudinous applications.

Herein, we developed an SBU regulating strategy to construct the MOF-based hetero-phase nanostructure for photocatalysis. Ti-MOFs are regarded as semiconductor photocatalysts and possess similar photocatalytic properties with TiO_2.[17] Among these, two crystal phases of Ti-MOFs (i.e., MIL-125 and COK) were both composed of titanium and 1,4-dicarboxybenzene (BDC). As one of the most common MOFs, MIL-125 was composed of Ti_8O_8 clusters and BDC, and its specific surface area was much larger than that of COK. In contrast, defect-rich Ti–O sheets acted as two-dimensional infinite SBUs in the framework of COK, which meant abundant catalytic sites in this novel phase. In addition, both the experimental and theoretical calculation results revealed that these two phases possessed different energy levels, and a Z-scheme homojunction could be constructed in COK/MIL-125 hetero-phase nanostructure, which could facilitate the separation of photogenerated electrons and holes. As a result, COK/MIL-125 possessed the best photocatalytic activity for hydrogen evolution, with H_2 yield of 3055.6 $\mu mol \cdot g^{-1} \cdot h^{-1}$, much higher than those of MIL-125 (416.6 $\mu mol \cdot g^{-1} \cdot h^{-1}$), COK (2054.3 $\mu mol \cdot g^{-1} \cdot h^{-1}$) and COK + MIL-125 (882.7 $\mu mol \cdot g^{-1} \cdot h^{-1}$). Not only that, by decorating amino groups on BDC ligands, the band structures of the two phases could be regulated, and the light absorbing region was broadened to visible-light region. Hence, the as-synthesized NH_2-COK/NH_2-MIL-125 realized the visible-light-driven photocatalytic hydrogen evolution (2277.9 $\mu mol \cdot g^{-1} \cdot h^{-1}$), which was also superior to the two single phases (i.e., NH_2-COK and NH_2-MIL-125). As for this kind of novel hetero-phase nanostructure, the capacity of charge transfer, porosity and metal catalytic sites could all be regulated by the SBUs. The last but not least, the energy levels could also be adjusted at the molecular level. Based on the above-mentioned, our work not only contributes to the crystal phase engineering research in MOFs, but also

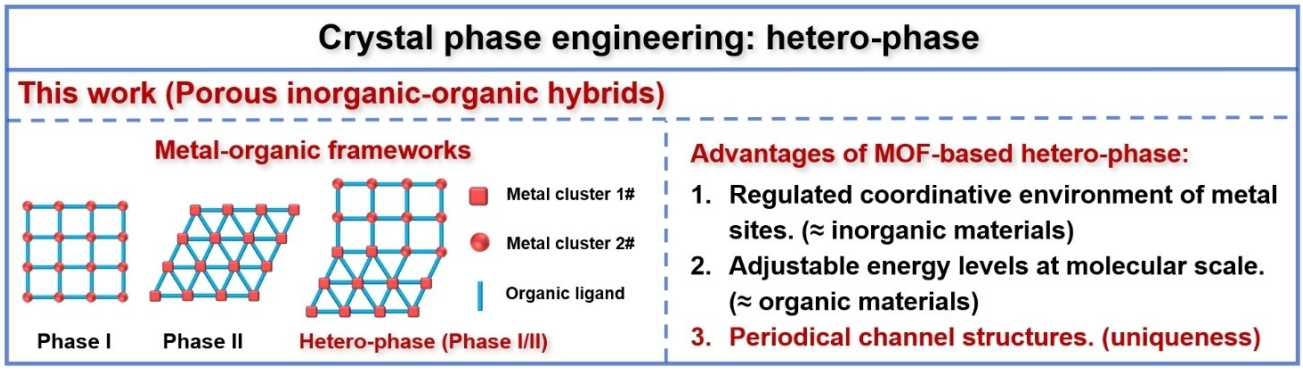

Figure 1. The schematic diagram of crystal phase engineering in material science and the hetero-phase composites. This work aims at constructing a novel kind of porous inorganic-organic hybrid hetero-phase, i.e., MOF-based hetero-phase.

provides a novel avenue for designing high-performance functional composites.

Results and Discussion

The two crystal phases of MOFs were both composed of titanium and BDC, and successfully prepared via the solvothermal approach, as shown in Figure 2a. Formic acid and acetic acid were employed as acid modulator to regulate the dynamic process of MOFs self-assembly,[14c] and hence COK and MIL-125 were successfully prepared, respectively. In the crystal structure of COK, the two-dimensional Ti–O sheet SBUs were constructed by μ_2–O bridged double chains of Ti(IV)O_6 octahedra, and the two adjacent Ti–O sheets were connected by BDC ligands to form a three-dimensional framework (Figure 2a). As for the other crystal phase (MIL-125), Ti_8O_8 cluster SBUs were the cyclic octamers of edge- and corner-sharing TiO_5(OH) octahedra, which were further linked by BDC to form a three-dimensional porous structure. Two kinds of cages in MIL-125 formed the octahedral and tetrahedral vacancies, which guaranteed the excellent mass transfer in this framework. Transmission electron microscopy (TEM) and scanning electron microscopy (SEM) images showed that the morphologies of COK and MIL-125 were woolen balls and disks, respectively (Figures S1–S4). The uniform morphology indicated the pure crystal structures of as-prepared samples. Following, the powder X-ray diffraction (PXRD) profiles of as-prepared COK and MIL-125 were both consistent with the refinement results, as shown in Figures S5 and S6. The above-mentioned results all confirmed that two kinds of crystal phases (i.e., COK and MIL-125) were successfully prepared.

Following, the physicochemical properties of COK and MIL-125 were further characterized. The Brunauer-Emmet-Teller (BET) measurement results revealed that the specific surface area of MIL-125 (1436.0 $m^2 \cdot g^{-1}$) was much higher than that of COK (119.9 $m^2 \cdot g^{-1}$), which was also consistent with their crystal structures (Figure S7 and Table S1). Thermal gravity (TG) results demonstrated that the thermal stability of COK was better than that of MIL-125 (Figure S8). As for the chemical stability, the crystal structure of COK could be maintained in an acidic aqueous solution (pH = 1) for 12 h, but the MIL-125 was totally destroyed and dissolved into the solution (Figures S9 and S10). When these

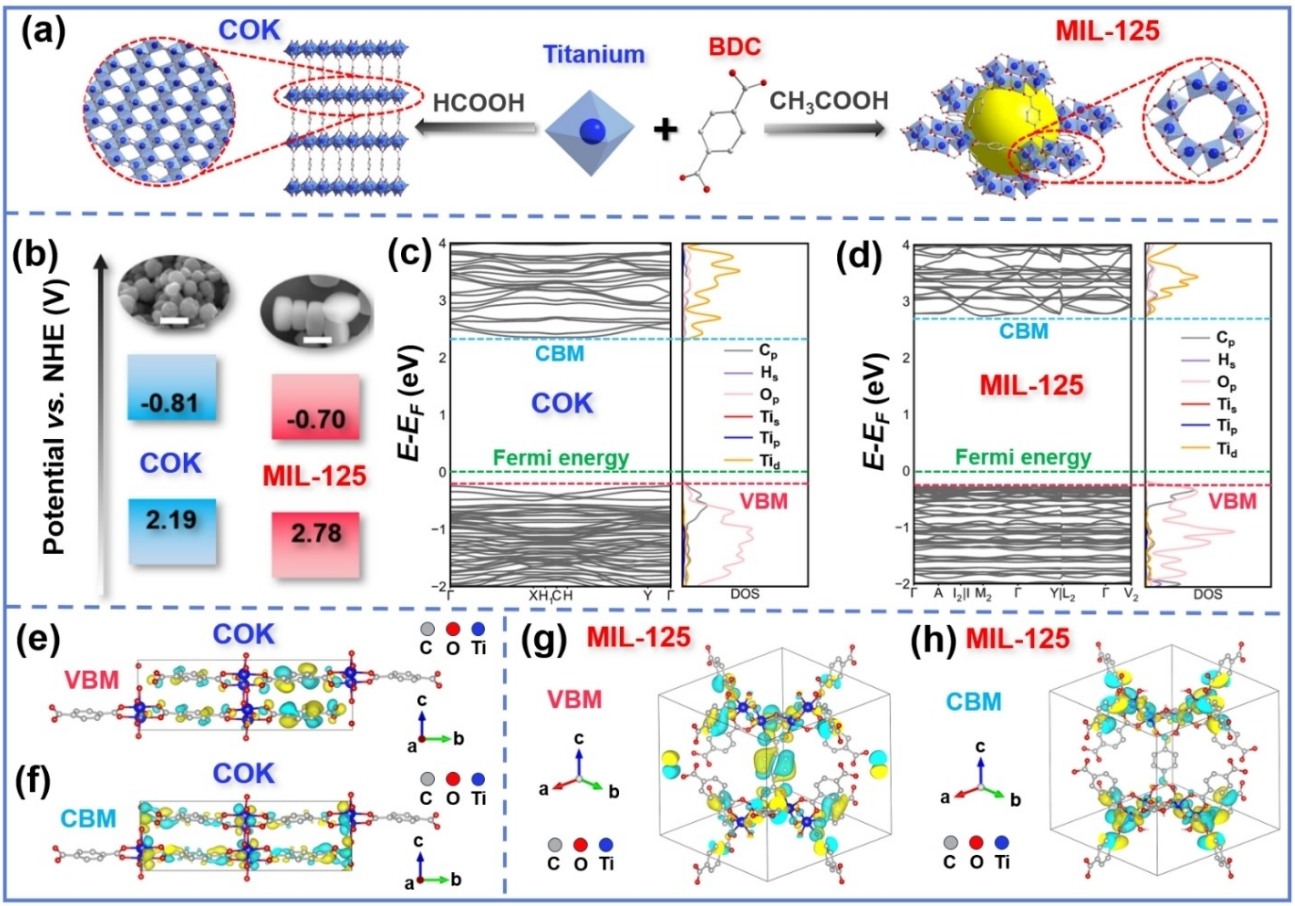

Figure 2. (a) Schematic diagram showing the synthesis of COK and MIL-125 via acid regulation. (b) The energy levels of COK and MIL-125 based on experimental results. Electronic band structure (left) and PDOS on orbitals (right) of COK (c) and MIL-125 (d). Visualization diagrams of VBM (e) and CBM (f) of COK in real space. Visualization diagrams of VBM (g) and CBM (h) of MIL-125 in real space. Hydrogen atoms are omitted for clarity.

samples were placed in alkaline solutions (pH = 12), the XRD profiles demonstrated that both COK and MIL-125 maintained their crystalline structures (Figure S11). Based on these results, both the thermal and chemical stabilities of COK were better than those of MIL-125. This might be attributed to the different SBUs of the two phases. The metal sites and kinetics of charge transfer in two phases were further studied by the electron paramagnetic resonance (EPR) and electrochemical impedance spectroscopy (EIS), respectively. In the EPR spectra (Figure S12), the strong signal at g = 2.002 for COK revealed the abundant oxygen vacancies in Ti–O sheet SBUs, but a negligible peak was observed in the profile of MIL-125. The results of X-ray photoelectron spectroscopy (XPS) showed that the content of oxygen vacancies in COK was indeed higher than that of MIL-125 (Figure S13). It was further demonstrated that COK possessed more open metal sites than MIL-125. As shown in Figure S14, compared with MIL-125, COK exhibited a smaller radius of semicircular arc in the Nyquist plot, signifying that the charge transfer in COK was more favorable than that in MIL-125. Based on the previous report, the electrical conductivity of MOFs was positively related to the dimensions of SBUs,[17] and hence the better charge transfer in COK was attributed to the two-dimensional Ti–O nanosheet SBUs.

Ti-MOF is a kind of semiconductor material, and thus its band structure is an important intrinsic property. The conduction band (E_C) of COK was characterized to be −0.81 V (vs. NHE) by Mott–Schottky plot, and the Tauc plot results revealed that the band gap (E_G) of COK was 3.00 eV (Figure S15). Then the valence band (E_V) was calculated as 2.19 V (vs. NHE). Similarly, the E_C, E_G and E_V of MIL-125 were determined as −0.70 V, 3.48 eV and 2.78 V, respectively (Figure S16). Then the energy levels of COK and MIL-125 were systematically summarized in Figure 2b. To comprehensively elucidate and gain a clear understanding of the correlations between crystal phases and band structures, the in-depth exploration of the electronic structures of COK and MIL-125 was conducted utilizing the PBEsol density function within the framework of density functional theory (DFT). As shown in Figures 2c and 2d, the electronic band structure and projected density of states (PDOS) calculations revealed that the Fermi levels of COK and MIL-125 were both close to their valence bands, revealing the p-type semiconductor behavior. Notably, the calculated band gap was 2.59 eV for COK and 3.02 eV for MIL-125, slightly smaller than the experimental results (Table S2), which was attributed to the inherent tendency of DFT calculations to underestimate band gaps.[18] The detailed analysis for the compositions of valence and conduction bands was conducted by scrutinizing PDOS with regards to elements and orbitals, and then the visualization diagrams showed valence band maximum (VBM) and conduction band minimum (CBM) wave functions in real space (Figures 2e–2h). Based on the results of PDOS, VBM, and CBM investigations, the p orbitals of C and O on organic ligands contributed to the valence bands. Additionally, the conduction bands of both COK and MIL-125 were mainly dependent on p orbitals of C and O in organic ligands, as well as d orbitals of Ti. This pattern reflects a consistent six-coordinated octahedral orbital hybridization coordination mode in both COK and MIL-125. Moreover, the energy gap (E_V−E_F) between VBM and Fermi level of COK (0.24 eV) was similar to that of MIL-125 (0.28 eV), attributing to the comparable p orbitals of C and O offered by the same organic ligand (i.e., BDC). Hence, it was further demonstrated that VBM of MOF was heavily dependent on the p orbitals of C and O. In contrast, the energy gap (E_C−E_F) between CBM and Fermi level of COK-BDC (2.35 eV) was significantly smaller than that of MIL-125 (2.74 eV), closely tied to the different SBUs in their frameworks. Hence, the the orbitals of Ti and O of SBUs played crucial roles in shaping the CBM.

Based on the above-mentioned results, the as-synthesized two phases of Ti-MOFs exhibited different physicochemical properties. MIL-125 with larger BET specific area possessed better mass transfer for substrate molecules. In contrast, the unique SBUs (i.e., two-dimensional infinite Ti–O sheet) endowed COK with abundant catalytic sites and more favorable channels for charge transfer, which meant the higher catalytic activity and better charge transfer within frameworks. The last but not the least, the band structures of Ti-MOFs could be regulated by the crystal phases. Hence, crystal phase engineering played an important role in modulating the intrinsic properties of MOFs.

Each phase of Ti-MOF possesses its unique advantages, and the MOF-based hetero-phase could not only combine their advantages, but also benefit the separation of photo-generated carriers via the homojunction at hetero-phase interface. Herein, via an acid regulating strategy, two phases of Ti-MOFs (i.e., COK and MIL-125) have been synthesized, and the most important is that COK and MIL-125 possessed different band structures. In thermodynamics, it is possible to construct Z-scheme homojunction at the hetero-phase interface between COK and MIL-125, which might be beneficial for optimizing the separation of photo-generated carriers.

Following, the COK/MIL-125 hetero-phase nanostructure was constructed by growing MIL-125 around the COK nanospheres via the interaction of coordination bonds (Figure 3a). The bright and dark field TEM images clearly showed that the COK nanospheres were incorporated in MIL-125 octahedron (Figures 3b and 3c). As shown in Figure S17, the HRTEM image further revealed the maintained crystal lattice of incorporated COK. Besides, as shown in Figure 3d, the characteristic peaks of MIL-125 and COK could be both observed in the XRD profile of as-prepared COK/MIL-125, signifying the presence of two phases in the as-prepared nanostructure. The SEM image of COK/MIL-125 also verified the successful preparation of hetero-phase nanostructures (Figure S18). However, as for the above-mentioned TEM and SEM images, the sample was only observed from a single direction, which preliminarily demonstrated that COK was embeded into MIL-125. To further reveal the unique hetero-structure of COK/MIL-125, the target sample should be observed from different angles. The sample was observed along with the clockwise (−20°, −40° and −50°) and anticlockwise (20°, 40° and 50°)

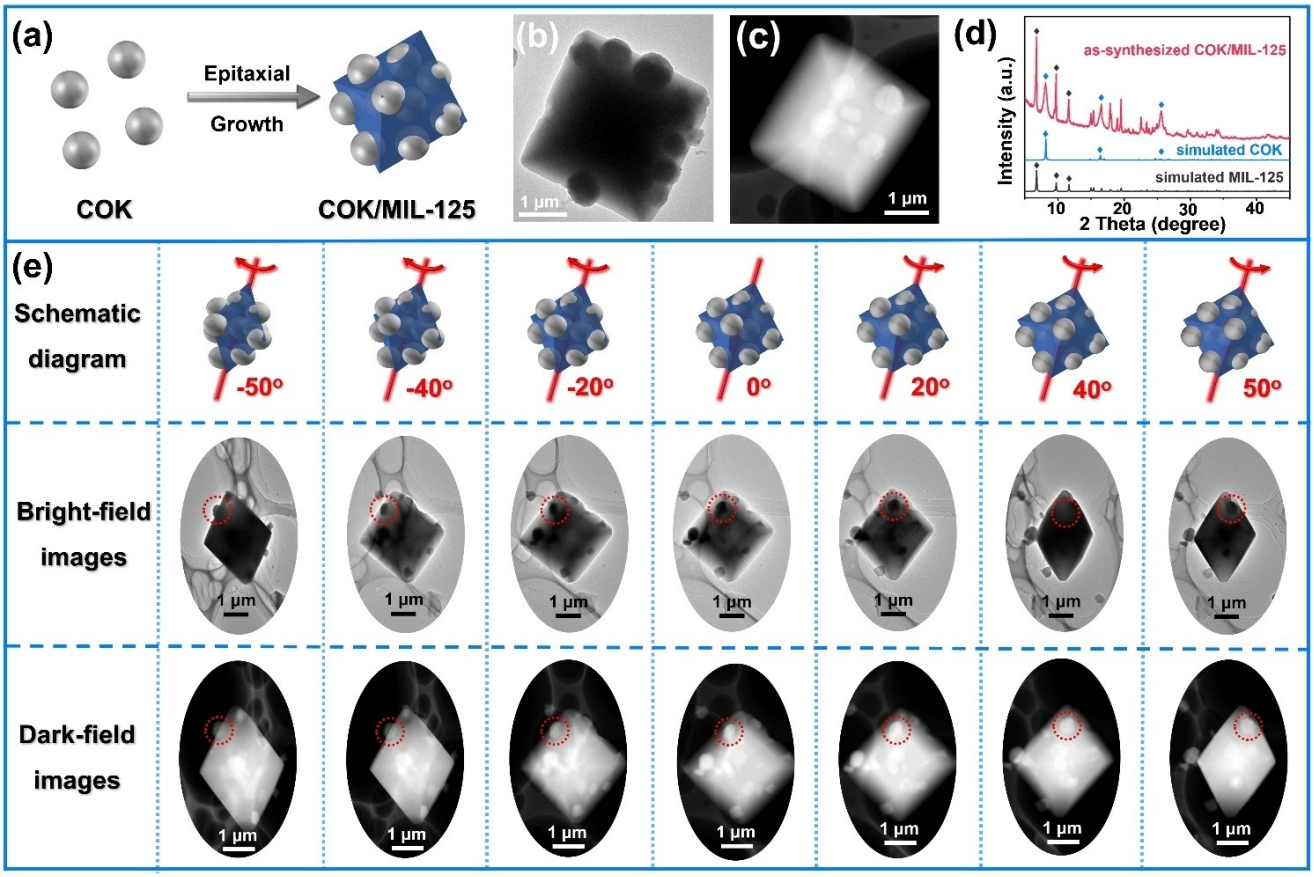

Figure 3. (a) Schematic diagram of preparing COK/MIL-125 hetero-phase. The bright-field TEM (b), dark-field TEM (c) images and XRD profile (d) of as-synthesized COK/MIL-125 hetero-phase nanostructure. (e) The TEM images of COK/MIL-125 viewed from different angles.

rotation, as shown in Figure 3e. These TEM images viewed from different angles showed that the target COK nanoparticle labeled in red circle was indeed incorporated in MIL-125, hence certifying that COK was incorporated into MIL-125 rather than on its surface. As shown in Figure S19, the BET measurement results revealed that the specific surface area of COK/MIL-125 ($600.0\ m^2 \cdot g^{-1}$) was higher than that of COK ($119.9\ m^2 \cdot g^{-1}$) but lower than that of MIL-125 ($1436.0\ m^2 \cdot g^{-1}$). In addition, the as-prepared COK/MIL-125 possessed similiar thermal stability with COK and MIL-125 (Figure S20). These results indicated that the COK/MIL-125 hetero-phase nanostructure was successfully synthesized and could be employed for further applications.

In the photocatalytic hydrogen evolution reaction (HER), the samples' light absorbing range is very important for their photocatalytic performance. Based on UV/Vis spectra, the light absorbing capacities of MIL-125, COK and COK/MIL-125 mainly covered on UV region (Figure 4a). Due to the large band gap, the photogenerated electrons and holes of COK or MIL-125 were mainly derived from UV radiation, and hence the full-spectrum radiation was employed in the photocatalytic HER. As shown in Figure 4b and Table S3, COK/MIL-125 hetero-phase showed the highest H_2 yield of $3055.6\ \mu mol \cdot g^{-1} \cdot h^{-1}$, in comparison with MIL-125 ($416.6\ \mu mol \cdot g^{-1} \cdot h^{-1}$) and COK ($2054.3\ \mu mol \cdot g^{-1} \cdot h^{-1}$). Besides, the physically mixed sample

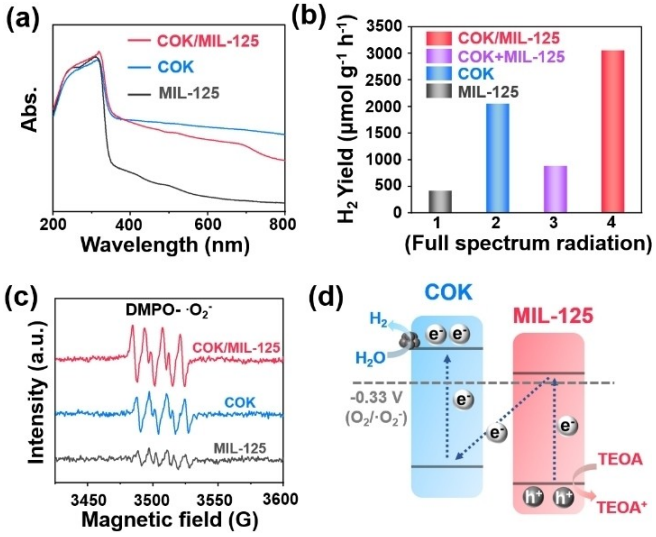

Figure 4. (a) UV/Vis spectra of MIL-125, COK and COK/MIL-125. (b) H_2 yields of MIL-125, COK, physical mixture sample (i.e., COK + MIL-125) and COK/MIL-125. (c) EPR measurements of MIL-125, COK, and COK/MIL-125. (d) The schematic diagram of Z-scheme homojunction in COK/MIL-125 hetero-phase.

(COK + MIL-125) was prepared as the counterpart sample (Figure S21 and S22), and only exhibited 882.7 umol·g^{-1}·h^{-1} H_2 yield much lower than that of COK/MIL-125, indicating that the unique hetero-phase nanostructure played an important role in improving the photocatalytic activity. The control experiments demonstrated that the illumination, MOF photocatalyst and sacrificial agent were all the essential factors for photocatalytic HER (Figure S23 and Table S4). In the absence of Pt, the H_2 yield was only 29.3 μmol·g^{-1}·h^{-1} much lower than that of normal condition. Hence, it was demonstrated that Pt as the co-catalysts played an important role in improving the photocatalytic hydrogen evolution performance. The XRD profiles of the COK, MIL-125 and COK/MIL-125 after photocatalytic tests were still consistent with those of fresh samples, demonstrating that the crystal structures of these MOF photocatalysts could be well maintained during photocatalysis (Figure S24). After photocatalysis, the TEM image of used COK/MIL-125 showed that COK was still incorporated in MIL-125, and HTREM images showed the maintained the crystal lattice of COK (Figure S25 and S26), which revealed the stable structure of COK/MIL-125. In the cyclic experiments, the photocatalytic activity of COK/MIL-125 could be maintained in 6 cycles (Figure S27), which further demonstrated its stability in photocatalysis.

Based on these results, the superior photocatalytic activity could be attributed to the hetero-structure of COK/MIL-125, and it was possible to construct Z-scheme homojunction at the hetero-phase interface between COK and MIL-125. For revealing reduction position for hydrogen evolution, the EPR analysis was employed to detect the spin active $^{\bullet}O_2^-$ species using 5,5-dimethyl-1-pyrroline N-oxide (DMPO) as the trapping agent. As shown in Figure 4c, the DMPO-$^{\bullet}O_2^-$ signal of COK was higher than that of MIL-125, and COK/MIL-125 showed the highest signal, indicating that photogenerated electron was finally transferred to COK for reduction reaction. Based on the ultraviolet photoelectron spectroscopy (UPS) results, working functions (WFs) of COK and MIL-125 were determined as 5.0 and 5.4 eV (Figure S28). After contact, the Fermi levels of COK and MIL-125 were equilibrated, and the internal electric field directed from COK to MIL-125 was formed. Due to the internal electric field, the photogenerated electrons transferred from MIL-125 to COK (Figure S29), further demonstrating the Z-scheme junction between COK and MIL-125. The schematic diagram of Z-scheme homojunction was shown in Figure 4d. Hence, the superior photocatalytic activity of COK/MIL-125 nanostructure was contributed to the Z-scheme homojunction at the hetero-phase interface.

The band gaps of COK, MIL-125 and COK/MIL-125 are so large that excited electrons and holes can not be photogenerated under visible-light radiation, which greatly impedes their further development. Hence, it is of significance to broaden the light absorbing range of MOFs for efficient photocatalysis. Based on the previous literatures,[19] it is an effective approach to broaden the range of light absorbing for MOFs via decorating organic ligands with amino functional groups.

In this work, we introduced a certain amount of NH_2-BDC into the framework of COK and MIL-125 to construct the mix-ligand (i.e., BDC and NH_2-BDC) MOFs. These MOFs containing NH_2-BDC were named as NH_2-COK, NH_2-MIL-125 and NH_2-COK/NH_2-MIL-125. TEM and SEM images showed that the morphologies of NH_2-COK and NH_2-MIL-125 still kept coarse yarn balls and octahedral analogues, respectively (Figures S30–S33). The PXRD profiles of these samples were also consistent with the simulated results (Figures S34 and S35). Based on the EPR results, the NH_2-COK possessed more oxygen vacancy than NH_2-MIL-125 (Figure S36), and BET results showed that the specific surface area of NH_2-MIL-125 was larger than that of NH_2-COK (Figures S37, S38 and Table S1). In the measurements of chemical stability, NH_2-COK showed better stability than NH_2-MIL-125 in the acid aqueous solution (Figures S39–S41). In general, the crystal structures of mix-ligand MOFs were still consistent with those of single-ligand MOFs, and their morphology and stability could also be maintained to some extent.

As for photocatalytic applications, the introduction of NH_2-BDC aims at regulating band structures of MOFs. The E_C of NH_2-COK was characterized to be −0.81 V (vs. NHE) by Mott–Schottky plot, and the Tauc plot revealed that the E_G of NH_2-COK was 2.74 eV (Figure S42). Then the E_V was calculated to be 1.93 V (vs. NHE). Similarly, the E_C, E_G and E_V of NH_2-MIL-125 could be determined to be −0.70 V, 2.73 eV and 2.03 V, respectively (Figure S43). The energy levels of NH_2-COK and NH_2-MIL-125 were summarized in Figure 5a.

Following, via a similar liquid epitaxial growth, NH_2-COK could also be incorporated into NH_2-MIL-125 (Figure 5b), and the HRTEM image showed the clear crystalline fringe on the surface of embedded NH_2-COK (Figure S44). As shown in Figure 5c, the energy dispersive X-ray spectroscopy (EDS) element mapping showed the even distribution of N in NH_2-COK/NH_2-MIL-125, which demonstrated the uniform introduction of NH_2-BDC in the hetero-phase nanostructure. Additionally, the XRD results showed that both the characteristic peaks of two phases could be observed in the profile of NH_2-COK/NH_2-MIL-125 (Figure 5d). These results indicated that the NH_2-COK/NH_2-MIL-125 hetero-phase nanostructure was successfully prepared. As shown in Figure S45, the specific surface area of NH_2-COK/NH_2-MIL-125 (489.9 $m^2 \cdot g^{-1}$) was higher than that of NH_2-COK (66.5 $m^2 \cdot g^{-1}$) but lower than that of NH_2-MIL-125 (1223.4 $m^2 \cdot g^{-1}$). UV/Vis spectra showed that these NH_2-groups-decorated samples possessed excellent light absorbing capacity in the visible-light range (Figure 5e). Hence, the following photocatalytic HER measurements were conducted under visible light. As expected, the samples without NH_2 groups (i.e., COK, MIL-125 and COK/MIL-125) were not capable of photocatalyzing hydrogen evolution under visible-light radiation (Figures S46 and Table S5). After the introduction of NH_2 groups, NH_2-MIL-125, NH_2-COK, physical mixture (NH_2-COK + NH_2-MIL-125) and hetero-phase NH_2-COK/NH_2-MIL-125 exhibited H_2 yields of 328.6, 1447.3, 398.3 and 2277.9 μmol·g^{-1}·h^{-1}, respectively (Figure 5f and Table S6). As expected, the hetero-phase

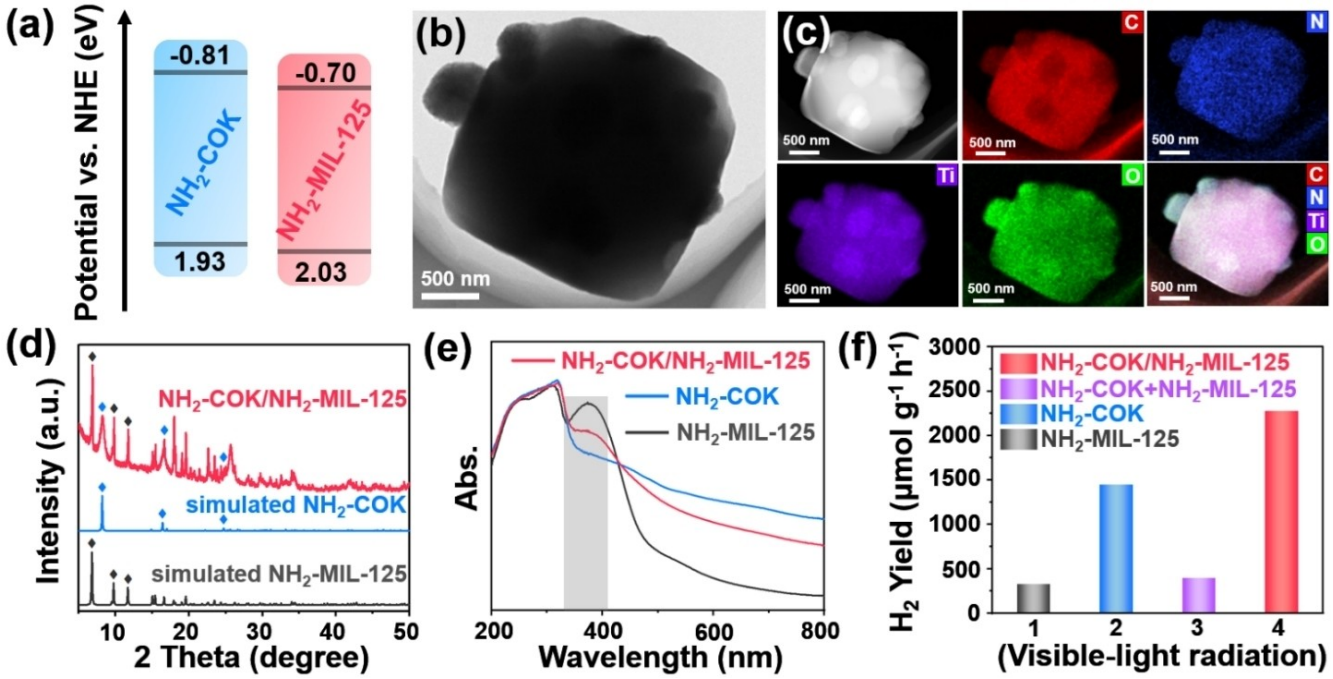

Figure 5. (a) The band structures of NH_2-COK and NH_2-MIL-125. (b) TEM image of NH_2-COK/NH_2-MIL-125 hetero-phase nanostructure. EDS element mapping (c) and XRD profile (d) of NH_2-COK/NH_2-MIL-125. UV/Vis spectra (e) and visible-light driven H_2 yields (f) of NH_2-MIL-125, NH_2-COK, physical mixture sample (NH_2-COK + NH_2-MIL-125) and NH_2-COK/NH_2-MIL-125 hetero-phase nanostructure.

nanostructure containing NH_2 groups possessed the highest photocatalytic activity. Under full-spectrum radiation, the H_2 yield of NH_2-COK/NH_2-MIL-125 (3924.0 $\mu mol \cdot g^{-1} \cdot h^{-1}$) was higher than that of COK/MIL-125 (3055.6 $\mu mol \cdot g^{-1} \cdot h^{-1}$), which could be ascribed to the enhanced visible-light absorption (Figure S47). Besides, the Z-scheme homojunction in NH_2-COK/NH_2-MIL-125 was also determined by EPR results (Figure S48), which played an important role in achieving the superior photocatalytic activity. After photocatalysis, the PXRD profiles of used MOF-based photocatalysts still kept consistent with those of fresh samples (Figure S49), signifying their stability during photocatalysis. In the cyclic experiments, the photocatalytic activity of NH_2-COK/NH_2-MIL-125 could be maintained in 6 cycles (Figure S50), which further demonstrated its stability in photocatalysis.

Based on these results, the band structures of components in MOF-based hetero-phase nanostructure can be regulated at the molecular scale via functionalizing organic ligands with NH_2 groups. Besides, it is further demonstrated that the hetero-phase structure is indeed beneficial for improving photocatalytic performance. In comparison with previous MOF-based photocatalyst, the as-synthesized MOF-based hetero-phase nanostructures also exhibited excellent photocatalytic activity (Table S7).

To reveal the superiority of MOF-based hetero-phase nanostructure, the kinetics of photogenerated carriers should be further studied. The photoluminescence (PL) spectra showed that the fluorescence intensity of NH2-COK/NH2-MIL-125 was the lowest in comparison with those of NH_2-COK and NH_2-MIL-125 (Figure 6a), demonstrating that the highest separation efficiency of photogenerated carriers in the hetero-phase. In the photocurrent measurements, the photocurrent density of the NH_2-COK/NH_2-MIL-125 was higher than those of NH_2-COK and NH_2-MIL-125 (Figure 6b), indicating that the hetero-phase structure was beneficial for facilitating charge transfer. Moreover, the values of semicircular radius of EIS Nyquist plots for these samples were in a gradually decreased order of NH_2-MIL-125 > NH_2-COK > NH_2-COK/NH_2-MIL-125 (Figure 6c), further revealing the effect of hetero-phase on boosting charge transfer. In the NH_2-COK/NH_2-MIL-125 hetero-phase nanostructure, the excellent charge separation efficiency would cause more photogenerated charges enriched on the surface of catalysts. The surface photovoltage (SPV) was directly related to the charge density on the surface of photocatalysts, which could be probed by the Kelvin probe force microscopy (KPFM). The contact potential difference changes (ΔCPD) were obtained by different SPV values between potential images in the dark and light. In comparison with those of NH_2-COK and NH_2-MIL-125, the ΔCPD value of NH_2-COK/NH_2-MIL-125 was the highest (Figures 6d–6f, S51 and S52), signifying the highest separation efficiency of photogenerated electrons and holes in NH_2-COK/NH_2-MIL-125. The similar phenomena also occurred in the measurement results of COK, MIL-125 and COK/MIL-125 (Figures S53–S59). In general, the above-mentioned evidences all demonstrated that the hetero-phase nanostructure was beneficial for improving the separation of photogenerated electrons and holes to realize the more efficient photocatalysis.

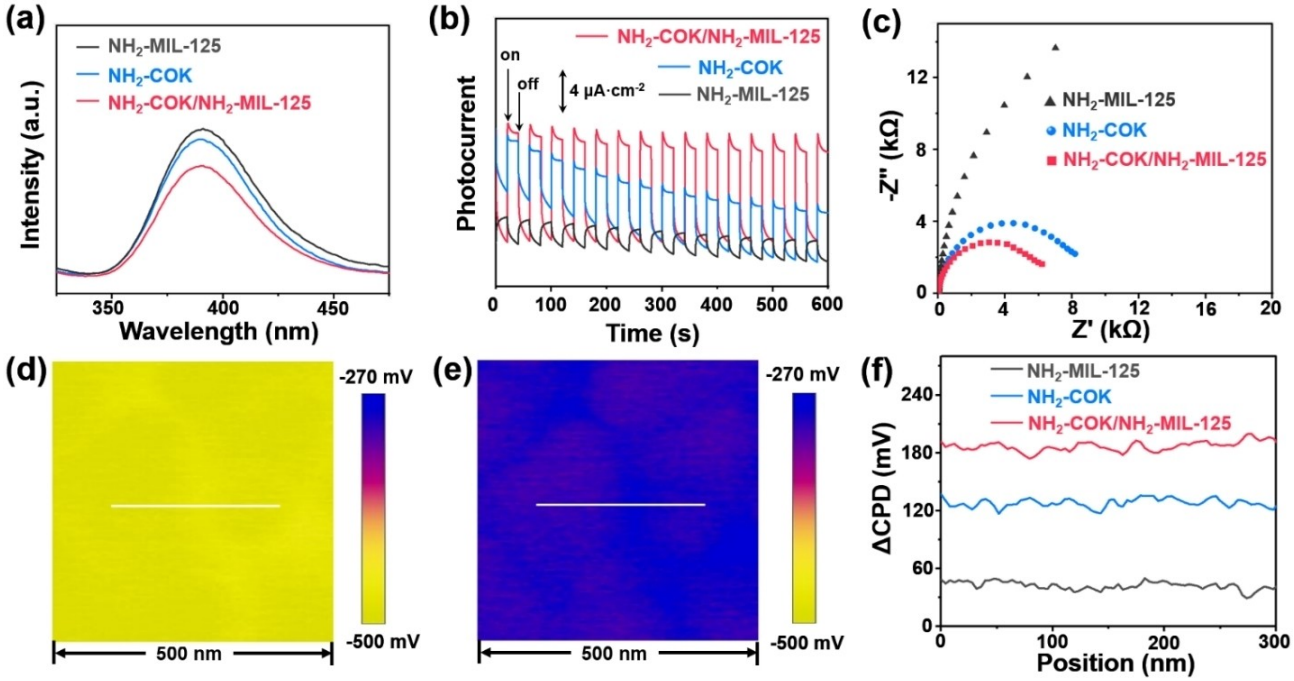

Figure 6. PL spectra (a), photocurrent measurements (b) and EIS Nyquist plots (c) of NH_2-MIL-125, NH_2-COK and NH_2-COK/NH_2-MIL-125. The differential SPV images of NH_2-COK/NH_2-MIL-125 between potential images (d) in dark and (e) under irradiation. (f) ΔCPD in dark and under illumination of NH_2-MIL-125, NH_2-COK and NH_2-COK/NH_2-MIL-125.

Conclusions

We developed an SBU regulating strategy to construct MOF-based hetero-phase nanostructure (i.e., COK/MIL-125). The two phases in this hetero-phase nanostructure possessed different physicochemical properties. As the common phase, MIL-125 was constructed by Ti_8O_8 clusters and BDC, forming a three-dimensional porous structure with a large specific area. As a novel phase, COK containing Ti–O sheet SBUs possessed excellent capacity of charge transfer and abundant catalytic sites. *Via* the liquid-phase epitaxial growth, COK was incorporated into MIL-125, and the COK/MIL-125 hetero-phase nanostructure was prepared. In the photocatalytic hydrogen evolution under full-spectrum radiation, COK/MIL-125 hetero-phase exhibited the highest H_2 yield than COK and MIL-125, in which the Z-scheme homojunction in hetero-phase boosted the separation of photogenerated carriers. After introducing NH_2-BDC, the light absorbing capacities of these MOF samples were broadened to visible light range. Under the radiation of visible light, the as-synthesized NH_2-COK/NH_2-MIL-125 still showed the best photocatalytic activity compared with NH_2-COK and NH_2-MIL-125. This MOF-based hetero-phase nanostructure not only possessed periodic porous channel, but also realized the molecular-scale regulation of band energy levels. Hence, the MOF-based hetero-phase nanostructure combined the features of traditional organic and inorganic based hetero-phase composites, and possessed its unique advantages. As a proof of concept, this work on constructing MOF-based hetero-phase paves a novel avenue for designing and constructing functional composites for various applications.

Supporting Information

The authors have cited additional references within the Supporting Information.

Acknowledgements

This work was supported by the National Key Research and Development Program of China (2022YFA1502902, 2022YFB3603800), National Natural Science Foundation of China (22205162, 22271218, 22071182), Tianjin Research Innovation Project for Postgraduate Students (2022SKY171).

Conflict of Interest

The authors declare no conflict of interest.

Keywords: crystal phase engineering · hetero-phase · metal–organic framework · photocatalysis · nanomaterials

[1] a) Y. Chen, Z. Lai, X. Zhang, Z. Fan, Q. He, C. Tan, H. Zhang, *Nat. Chem. Rev.* **2020**, *4*, 243–256; b) M. Zhao, Y. Xia,

Nat. Rev. Mater. **2020**, *5*, 440–459; c) P. Yu, Y. Zhen, H. Dong, W. Hu, *Chem* **2019**, *5*, 2814–2853.
[2] a) X. Yin, C. S. Tang, Y. Zheng, J. Gao, J. Wu, H. Zhang, M. Chhowalla, W. Chen, A. T. S. Wee, *Chem. Soc. Rev.* **2021**, *50*, 10087–10115; b) H. Yang, S. W. Kim, M. Chhowalla, Y. H. Lee, *Nat. Phys.* **2017**, *13*, 931–937.
[3] a) Z. Zhang, L, Jiang, C. Cheng, Y. Zhen, G. Zhao, H. Geng, Y. Yi, L. Li, H. Dong, Z. Shuai, W. Hu, *Angew. Chem.* **2016**, *128*, 5292–5295; b) J. E. Park, M. Son, M. Hong, G. Lee, H. C. Choi, *Angew. Chem.* **2012**, *124*, 6489–6494; c) P. He, Z. Tu, G. Zhao, Y. Zhen, H. Geng, Y. Yi, Z. Wang, H. Zhang, C. Xu, J. Liu, X. Lu, X. Fu, Q. Zhao, X. Zhang, D. Ji, L. Jiang, H. Dong, W. Hu, *Adv. Mater.* **2015**, *27*, 825–830; d) G. Barbarella, M. Zambianchi, L. Antolini, P. Ostoja, P. Maccagnani, A. Bongini, E. A. Marseglia, E. Tedesco, G. Gigli, R. Cingolani, *J. Am. Chem. Soc.* **1999**, *121*, 8920–8926.
[4] a) M. Chhowalla, H. S. Shin, G. Eda, L. Li, K. P. Loh, H. Zhang, *Nat. Chem. Rev.* **2013**, *5*, 263–275; b) J. Yin, Z. Yin, J. Jin, M. Sun, B. Huang, H. Lin, Z. Ma, M. Muzzio, M. Shen, C. Yu, H. Zhang, Y. Peng, P. Xi, C. H. Yan, S. Sun, *J. Am. Chem. Soc.* **2021**, *143*, 15335–15343.
[5] a) L. Liu, J. Wu, L. Wu, M. Ye, X. Liu, Q. Wang, S. Hou, P. Lu, L. Sun, J. Zheng, L. Xing, L. Gu, X. Jiang, L. Xie, L. Jiao, *Nat. Mater.* **2018**, *17*, 1108–1114; b) Y. Wang, W. Zhai, Y. Ren, Q. Zhang, Y. Yao, S. Li, Q. Yang, X. Zhou, Z. Li, B. Chi, J. Liang, Z. He, L. Gu, H. Zhang, *Adv. Mater.* **2023**, *16*, 2307269.
[6] a) J. Zhang, Q. Xu, Z. Feng, M. Li, C. Li, *Angew. Chem. Int. Ed.* **2008**, *47*, 1766–1769; b) D. O. Scanlon, C. W. Dunnill, J. Buckeridge, S. A. Shevlin, A. J. Logsdail, S. M. Woodley, C. R. A. Catlow, M. J. Powell, R. G. Palgrave, I. P. Parkin, G. W. Watson, T. W. Keal, P. Sherwood, A. Walsh, A. A. Sokol, *Nat. Mater.* **2013**, *12*, 798–801.
[7] V. Coropceanu, J. Cornil, D. Fiho, Y. Olivier, R. Sibey, J. Brédas, *Chem. Rev.* **2007**, *107*, 926–952.
[8] Y. Yao, D. S. He, Y. Lin, X. Feng, X. Wang, P. Yin, X. Hong, G. Zhou, Y. Wen, Y. Li, *Angew. Chem. Int. Ed.* **2016**, *55*, 5501–5505.
[9] a) C. Avendano, Z. Zhang, A. Ota, H. Zhao, K. R. Dunbar, *Angew. Chem. Int. Ed.* **2011**, *50*, 6543–6547; b) R. A. Heintz, H. Zhao, X. Ouyang, G. Grandinetti, J. Cowen, K. Dunbar, *Inorg. Chem.* **1999**, *38*, 144–156.
[10] a) Q. Yang, Q. Xu, H. Jiang, *Chem. Soc. Rev.* **2017**, *46*, 4774–4808; b) H. Furukawa, K. E. Cordova, M. O'Keeffe, O. M. Yaghi, *Science* **2013**, *341*, 1230444; c) K. Yuan, T. Song, X. Zhu, B. Li, B. Han, L. Zheng, J. Li, X. Zhang, W. Hu, *Small* **2019**, *15*, 1804845; d) K. Yuan, T. Song, C. Yang, J. Guo, Q. Sun, Y. Zou, F. Jiao, L. Li, X. Zhang, H. Dong, L. Li, W. Hu, *J. Am. Chem. Soc.* **2021**, *143*, 17526–17534; e) K. Yuan, T. Song, D. Wang, X. Zhang, X. Gao, Y. Zou, H. Dong, Z. Tang, W. Hu, *Angew. Chem. Int. Ed.* **2018**, *130*, 5810–5815; f) A. Dey, J. Pradhan, S. Biswas, F. Rahimi, K. Biswas, T. K. Maji, *Angew. Chem. Int. Ed.* **2024**, e202315596; g) A. Ghosh, S. Karmakar, F. A. Rahimi, R. S. Roy, S. Nath, U. K. Gautam, T. K. Maji, *ACS Appl. Mater. Interfaces* **2022**, *14*, 25220–25231.
[11] T. A. Makal, A. A. Yakovenko, H. C. Zhou, *J. Phys. Chem. Lett.* **2011**, *2*, 1682–1689.
[12] a) M. Zhao, K. Yuan, Y. Wang, G. Li, J. Guo, L. Gu, W. Hu, H. Zhao, Z. Tang, *Nature* **2016**, *5369*, 76–80; b) K. Yuan, T. Song, D. Wang, Y. Zou, J. Li, X. Zhang, Z. Tang, W. Hu, *Nanoscale* **2018**, *10*, 1591–1597; c) X. Zu, Y. Zhao, X. Li, R. Chen, W. Shao, L. Li, P. Qiao, W. Yan, Y. Pan, Q. Xu, J. Zhu, Y. Sun, Y. Xie, *Angew. Chem.* **2023**, *135*, e202215247; d) K. Liu, Z. Meng, Y. Fang, H. Jiang, *eScience* **2023**, *3*, 100133; e) D. Yang, X. Wang, *SmartMat.* **2022**, *3*, 54–67; f) S. Karmakar, S. Barman, F. A. Rahimi, D. Rambabu, S. Nath, T. K. Maji, *Nat. Commun.* **2023**, *14*, 4508.
[13] a) Y. Liu, C. Chen, J. Valdez, D. M. Meira, W. He, Y. Wang, C. Harnagea, Q. Lu, T. Guner, H. Wang, C. Liu, Q. Zhang, S. Huang, A. Yurtsever, M. Chaker, D. Ma, *Nat. Commun.* **2021**, *12*, 1231; b) X. Zhou, J. Dong, Y. Zhu, L. Liu, Y. Jiao, H. Li, Y. Han, K. Davey, Q. Xu, Y. Zheng, S. Qiao, *J. Am. Chem. Soc.* **2021**, *143*, 6681–6690.
[14] a) J. Lyu, X. Gong, S. Lee, K. Gnanasekaran, X. Zhang, M. C. Wasson, X. Wang, P. Bai, X. Guo, N. C. Gianneschi, O. K. Farha, *J. Am. Chem. Soc.* **2020**, *142*, 4609–4615; b) S. Lo, L. Feng, K. Tan, Z. Huang, S. Yuan, K. Wang, B. Li, W. Liu, G. S. Day, S. Tao, C. Yang, T. Luo, C. Lin, S. Wang, S. J. L. Billinge, K. Lu, Y. J. Chabal, X. Zou, H. Zhou, *Nat. Chem.* **2020**, *12*, 90–97; c) D. Jiang, C. Huang, J. Zhu, P. Wang, Z. Liu, D. Fang, *Coord. Chem. Rev.* **2021**, *444*, 214064.
[15] S. Wang, T. Kitao, N. Guillou, M. Wahiduzzaman, C. M. Corcos, F. Nouar, A. Tissot, L. Binet, N. Ramsahye, S. Devautour-Vinot, S. Kitagawa, S. Seki, Y. Tsutsui, V. Briois, N. Steunou, G. Maurin, T. Uemura, C. Serre, *Nat. Commun.* **2018**, *9*, 1660.
[16] S. Zhao, Y. Wang, J. Dong, C. T. He, H. Yin, P. An, K. Zhao, X. Zhang, C. Gao, L. Zhang, J. Lv, J. Wang, J. Zhang, A. M. Khattak, N. A. Khan, Z. Wei, J. Zhang, S. Liu, H. Zhao, Z. Tang, *Nat. Energy* **2016**, *1*, 16184.
[17] Y. Yan, C. Li, Y. Wu, J. Gao, Q. Zhang, *J. Mater. Chem. A* **2020**, *8*, 15245–15270.
[18] a) H. Cheng, H. Lv, J. Cheng, L. Wang, X. Wu, H. Xu, *Adv. Mater.* **2022**, *34*, 2107480; b) P. Ayala, S. Naghdi, S. P. Nandan, S. N. Myakala, J. Rath, H. Saitom, P. Guggenberger, L. Lakahanlal, F. Kleitz, M. C. Toroker, A. Cherevan, D. Eder, *Adv. Energy Mater.* **2023**, *13*, 2300961; c) Á. García, R. Valero, F. Illas, *J. Phys. Chem. C* **2017**, *121*, 18862–1886; d) H. Xiao, J. Kheli, W. A. Goddard, *J. Phys. Chem. Lett.* **2011**, *2*, 212–217.
[19] M. B. Chambers, X. Wang, L. Ellezam, O. Ersen, M. Fontecave, C. Sanchez, L. Rozes, C. Mellot-Draznieks, *J. Am. Chem. Soc.* **2017**, *139*, 8222–8228.

Manuscript received: February 6, 2024
Accepted manuscript online: April 8, 2024
Version of record online: May 29, 2024